

ARTICLE OPEN



Symmetry of the emergent inductance tensor exhibited by magnetic textures

Soju Furuta¹, Wataru Koshibae² and Fumitaka Kagawa^{1,2}✉

Metals hosting gradually varying spatial magnetic textures are attracting attention as a new class of inductors. Under the application of an alternating current, the spin-transfer-torque effect induces oscillating dynamics of the magnetic texture, which subsequently yields the spin-motive force as a back action, resulting in an inductive voltage response. In general, a second-order tensor representing a material's response can have an off-diagonal component. However, it is unclear what symmetries the emergent inductance tensor has and also which magnetic textures can exhibit a transverse inductance response. Here, we reveal both analytically and numerically that the emergent inductance tensor should be a symmetric tensor in the so-called adiabatic limit. By considering this symmetric tensor in terms of symmetry operations that a magnetic texture has, we further characterize the magnetic textures in which the transverse inductance response can appear. This finding provides a basis for exploring the transverse response of emergent inductors, which has yet to be discovered.

npj Spintronics (2023)1:3; <https://doi.org/10.1038/s44306-023-00001-4>

INTRODUCTION

An inductor is a component that exhibits an inductive counter-electromotive force, V , under a time-varying electric current, I , following

$$V = L \frac{dI}{dt}, \quad (1)$$

where L denotes the inductance. The electric work done by the external power supply, IV , is hence

$$\int dt IV = \int dt IL \frac{dI}{dt} = \int d\left(\frac{1}{2}LI(t)^2\right), \quad (2)$$

which shows that the inductor stores an energy of $\frac{1}{2}LI^2$. Thus, it can also be said that an inductor is a component that can store an energy of $\Delta E = \frac{1}{2}LI^2$, under the application of an electric current. A textbook example is a solenoidal inductor, which stores energy as a magnetic-field energy¹. Other inductors possess similar energy-storing properties. An established example is the so-called kinetic inductor, in which the energy is stored as the kinetic energy of mobile charge carriers. When considering the Drude model of conduction electrons, one can immediately find that the inductance defined using the imaginary part of the angular-frequency (ω)-dependent resistivity, $\rho(\omega)$, agrees with the inductance defined using the total kinetic energy of electrons².

Recently, a new class of inductors, now referred to as emergent inductors, has been proposed theoretically³ and confirmed experimentally^{4–6}. In these inductors, the flowing conduction electrons exert a spin-transfer torque (STT)^{7–10} on the underlying magnetic texture; as a result, the magnetic texture exhibits time-dependent elastic deformations under an AC electric current in the linear-response regime. Such current-induced magnetic-texture dynamics exert a back action on the flowing conduction electrons, yielding the so-called spin-motive force or emergent electric field (EEF)^{11–15}. This phenomenon can be derived microscopically in terms of the so-called spin-Berry phase or the effective $U(1)$ gauge field, and the resulting EEF can be described

by

$$e_i(\mathbf{r}, t) = \frac{\hbar}{2|e|} \mathbf{m}(\mathbf{r}, t) \cdot [\partial_i \mathbf{m}(\mathbf{r}, t) \times \partial_t \mathbf{m}(\mathbf{r}, t)], \quad (3)$$

where $e(>0)$ is the elementary charge, $\mathbf{m}(\mathbf{r}, t)$ is the unit vector of the local magnetic moment at position \mathbf{r} and time t , and ∂_i ($i = x, y, z$) and ∂_t denote spatial and time derivatives, respectively (when the conduction-electron spins are not fully polarized, the so-called spin-polarization factor P is further multiplied on the right-hand side of Eq. (3)^{12,15}). It has been numerically demonstrated that in the so-called adiabatic limit (i.e., $\beta = 0$; see the “Methods” section), the inductance value defined using the EEF under an AC electric current quantitatively agrees with that defined using the current-induced magnetic-texture-deformation energy¹⁶. Thus, in the adiabatic limit, the emergent inductance is well defined, and both the electric and energetic responses are correctly captured by Eq. (1). On the other hand, when nonadiabaticity is concerned (i.e., $\beta \neq 0$), the inductance values derived independently from the two definitions do not match, implying that the system responses are beyond the framework of Eq. (1) and hence the inductance interpretation does not apply¹⁶.

An interesting aspect of emergent inductors is that the inductive electric response is potentially not limited to the applied current direction but may also appear along the perpendicular directions, as inferred from Eq. (3). Thus, in general, the emergent inductance, when it is well defined, should be represented by a tensor: $V_i = L_{ij} \frac{dI_j}{dt}$ ($i, j = x, y$) or

$$\begin{pmatrix} V_x \\ V_y \end{pmatrix} = \begin{pmatrix} L_{xx} & L_{xy} \\ L_{yx} & L_{yy} \end{pmatrix} \frac{d}{dt} \begin{pmatrix} I_x \\ I_y \end{pmatrix}. \quad (4)$$

In classical electrodynamics, such an inductance tensor with $i, j = 1, 2$ may be introduced to describe two mutually coupled coils, 1 and 2. It, therefore, appears that an emergent inductor possesses a function similar to that of a coupled classical inductor system. However, such an intuitive analogy requires careful consideration because the microscopic mechanism is quite

¹Department of Physics, Tokyo Institute of Technology, Tokyo 152-8551, Japan. ²RIKEN Center for Emergent Matter Science (CEMS), Wako 351-0198, Japan.

✉email: kagawa@phys.titech.ac.jp

different between classical and emergent inductors. For instance, in a coupled classical inductor system, one can analytically express the mutual inductance and find $L_{12} = L_{21} \equiv M^1$; moreover, the fact that the coupled system stores a positive energy in the quadratic form of $\frac{1}{2}L_{11}I_1^2 + \frac{1}{2}L_{22}I_2^2 + MI_1I_2$ for arbitrary values of I_1 and I_2 leads to a constraint, $L_{11}L_{22} \geq M^2$ ¹⁷, in addition to the obvious one, $L_{11}, L_{22} \geq 0$. Such classical electrodynamics considerations, however, are not helpful for emergent inductors consisting of an arbitrary spin texture including disorder, and thus, the relation between L_{xy} and L_{yx} appears to be nontrivial.

When considering the nature of L_{ij} , it is instructive to review the resistivity tensor, ρ_{ij} , as a textbook example. Note that any second-order tensor, K_{ij} , can always be decomposed into a symmetric part, K_{ij}^S , and an antisymmetric part, K_{ij}^A , namely, $K_{ij} = K_{ij}^S + K_{ij}^A$ with $K_{ij}^S = (K_{ij} + K_{ji})/2$ and $K_{ij}^A = (K_{ij} - K_{ji})/2$. In the case of ρ_{ij} , the symmetric part represents dissipative transport, whereas the antisymmetric part represents nondissipative transport, that is, the Hall resistivity. Thus, the symmetric and antisymmetric parts of ρ_{ij} have their own physical meanings with quite different characteristics. Therefore, the symmetry of the emergent inductance tensor is also an important issue in understanding the underlying physics.

In this paper, focusing on the adiabatic limit, in which the emergent inductance is well defined by Eq. (1)¹⁶, we aim to reveal the symmetry of the emergent inductance tensor and discuss the physical implications of the revealed symmetry. Our approach is two-fold. First, we consider the tensor-expressed circuit equation [Eq. (4)] in detail and draw a conclusion regarding the symmetry of L_{ij} ; this also enables us to discuss how the inductor tensor should behave under the time-reversal operation. Second, we numerically investigate L_{ij} for various magnetic textures using micromagnetic simulations. These two approaches consistently show that L_{ij} is a symmetric tensor (that is, $L_{xy} = L_{yx}$) and L_{ij} is even under the time-reversal operation. By combining the numerical results and symmetry arguments, we also find what kinds of magnetic textures can or cannot exhibit a transverse emergent inductance, L_{yx} . We note that the present conclusion is for the case where the emergent inductance is well-defined (i.e., the adiabatic limit, $\beta = 0$). The effect of nonadiabaticity (i.e., $\beta \neq 0$), which makes the emergent inductance ill-defined¹⁶, is discussed in the Supplementary Note 1.

RESULTS

Considerations for the circuit equation

We discuss the consequences that are prescribed in the tensor-expressed circuit equation, Eq. (4). Following the general arguments on a second-order tensor, we decompose L_{ij} into symmetric and antisymmetric parts: $L_{ij} = L_{ij}^S + L_{ij}^A$, or explicitly,

$$\begin{pmatrix} L_{xx} & L_{xy} \\ L_{yx} & L_{yy} \end{pmatrix} = \begin{pmatrix} L_{xx}^S & L_{xy}^S \\ L_{xy}^S & L_{yy}^S \end{pmatrix} + \begin{pmatrix} 0 & L_{xy}^A \\ -L_{xy}^A & 0 \end{pmatrix}. \quad (5)$$

To gain insight into the physical meaning of the symmetric and antisymmetric tensors, we consider the work done by the power source along a closed loop in the I_x - I_y plane, which is expressed as:

$$\oint dt (I_x V_x + I_y V_y) = \oint d \left(\frac{1}{2} L_{xx}^S I_x^2 + \frac{1}{2} L_{yy}^S I_y^2 + L_{xy}^S I_x I_y \right) + \oint dt L_{xy}^A \left(I_x \frac{dI_y}{dt} - I_y \frac{dI_x}{dt} \right). \quad (6)$$

Note that the first term in the right-hand side consists of only the symmetric tensor components and the integrand takes the form of a total derivative; hence, the contour integral results in zero. The expression, $\frac{1}{2} L_{xx}^S I_x^2 + \frac{1}{2} L_{yy}^S I_y^2 + L_{xy}^S I_x I_y$, is essentially the same as that derived for mutually coupled classical inductors, representing energy stored in the emergent inductor under a current. In

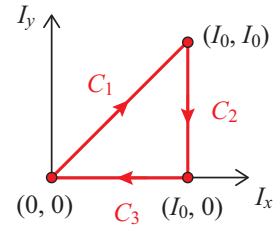


Fig. 1 A specific closed loop used to prove the absence of the antisymmetric components of an inductance tensor.

contrast, the second term consists of only the antisymmetric-tensor components, and the integrand is not the form of a total derivative, indicating that the second term is non-zero and dependent on the path. These features imply that L_{xy}^A is associated with a non-conserved quantity.

To see the consequences of the antisymmetric component L_{xy}^A more clearly, it is helpful to consider a specific closed path for the integral(s) of Eq. (6). Suppose $L_{xy}^A > 0$; we consider a specific cycle C that consists of three paths, C_1 , C_2 , and C_3 , as shown in Fig. 1: $(I_x, I_y) = (0, 0) \xrightarrow{C_1} (I_0, I_0) \xrightarrow{C_2} (I_0, 0) \xrightarrow{C_3} (0, 0)$ with constraints of $I_x = I_y$ on C_1 , $I_x = I_0$ on C_2 , and $I_y = 0$ on C_3 . Thus, taking the contour integral along the cycle in the clockwise direction results in:

$$\oint_C dt (I_x V_x + I_y V_y) = -L_{xy}^A I_0^2 < 0. \quad (7)$$

The result indicates that if a positive L_{xy}^A were present, the power source could acquire energy by cycling the closed loop. Such behavior is obviously not allowed for a passive element, such as a stable material. Similarly, one can consider the case of $L_{xy}^A < 0$, and the same conclusion can be drawn by considering the same closed loop C but in the counterclockwise direction. Thus, Eq. (4) concludes that even for the case of an emergent inductor, the inductance tensor cannot have an antisymmetric component; that is, $L_{xy}^A = 0$, and an emergent inductor tensor should be a symmetric tensor (below, we therefore omit the superscript, S),

$$L_{xy} = L_{yx} \equiv L_{tr}. \quad (8)$$

Hence, the energy stored in an emergent inductor under current is found to be expressed by $\frac{1}{2} L_{xx} I_x^2 + \frac{1}{2} L_{yy} I_y^2 + L_{tr} I_x I_y$, and for this quadratic form to be nonnegative, L_{ij} should satisfy

$$L_{xx} L_{yy} \geq (L_{tr})^2, \quad (9)$$

in addition to $L_{xx}, L_{yy} \geq 0$ ¹⁶.

Thus, although the microscopic mechanism is quite different between classical and emergent inductors, it turns out that there is no difference in the constraints that inductance tensors should satisfy. These characteristics are implicitly prescribed by the relation between voltage and current, Eq. (4), not depending on the microscopic mechanism for inductors.

Having established the symmetry of L_{ij} , we can discuss the behavior of L_{ij} under the time-reversal operation. Since an emergent inductance arises from a magnetic texture $\{\mathbf{m}(\mathbf{r})\}$, the behavior of an emergent inductance under the time-reversal operation is an interesting issue. In fact, in experiments, the magnetic-field (\mathbf{B})-dependence of an emergent inductance has been frequently investigated⁴⁻⁶. To incorporate a case where $\{\mathbf{m}(\mathbf{r})\}$ shows hysteretic behavior with respect to changes in \mathbf{B} , L_{ij} may be expressed as a function with $\{\mathbf{m}(\mathbf{r})\}$ and \mathbf{B} as variables. Note that regardless of the details of the variables, L_{ij} should be a symmetric tensor as discussed above, and hence, $L_{ij}(\mathbf{B}, \{\mathbf{m}(\mathbf{r})\}) = L_{ji}(\mathbf{B}, \{\mathbf{m}(\mathbf{r})\})$ should always be satisfied. Moreover, with respect to the complex resistivity, Onsager's reciprocal theorem concludes

$\text{Im} \rho_{ij}(\omega, \mathbf{B}, \{\mathbf{m}(\mathbf{r})\}) = \text{Im} \rho_{ij}(\omega, -\mathbf{B}, \{-\mathbf{m}(\mathbf{r})\})$ (the real part also satisfies the same relation)¹⁸; hence, the inductance tensor should also satisfy $L_{ij}(\mathbf{B}, \{\mathbf{m}(\mathbf{r})\}) = L_{ij}(-\mathbf{B}, \{-\mathbf{m}(\mathbf{r})\})$. By combining the two relations regarding L_{ij} , one can thus conclude

$$L_{ij}(\mathbf{B}, \{\mathbf{m}(\mathbf{r})\}) = L_{ij}(-\mathbf{B}, \{-\mathbf{m}(\mathbf{r})\}). \quad (10)$$

This relation indicates that L_{ij} is even under time reversal, or equivalently, L_{ij} is a polar symmetric tensor. In particular, we note $L_{yx}(\mathbf{B}, \{\mathbf{m}(\mathbf{r})\}) = L_{yx}(-\mathbf{B}, \{-\mathbf{m}(\mathbf{r})\})$, distinct from the Hall resistivity, which satisfies $\rho_{yx}(\mathbf{B}, \{\mathbf{m}(\mathbf{r})\}) = -\rho_{yx}(-\mathbf{B}, \{-\mathbf{m}(\mathbf{r})\})$. For this reason, we call L_{yx} the transverse inductance, not the Hall inductance.

Micromagnetic simulations

To observe the symmetry of the inductance tensor of emergent inductors, we consider magnetic textures that slowly vary in space; for such magnetic textures, the EEF can be calculated according to Eq. (3). We further consider the pinned regime, in which a magnetic texture does not exhibit a steady flow under a DC electric current^{19–28}. The procedure for calculating the emergent inductance arising from a slowly varying magnetic texture in the pinned regime is detailed in the literature¹⁶ and also in the “Methods” section. We consider a spin Hamiltonian based on the continuum approximation that can exhibit helical and skyrmion lattice (SkL)^{29–32} magnetic textures and calculate the current-induced dynamics of a magnetic texture by numerically solving the Landau–Lifshitz–Gilbert (LLG) equation³³ (see the “Methods” section). To be more specific, the magnetic-texture dynamics under the application of an AC current along the x -direction are calculated by micromagnetic simulation; then, by referring to Eq. (3), the time-dependent EEFs along both the x - and y -directions are further derived; and finally, by referring to Eq. (4), L_{xx} and L_{yx} are obtained. Similarly, we obtain L_{yy} and L_{xy} by simulating the case of an AC current along the y -direction. The emergent inductance L_{ij} depends on the system size in the form of $L_{ij} = \tilde{L}_{ij} \frac{\ell}{S}$, where \tilde{L}_{ij} , ℓ , and S represent the normalized inductance (we call it “inductivity”), system length, and system cross-section area. Below, we, therefore, present \tilde{L}_{ij} , rather than the system-size-dependent L_{ij} . The inductivity tensor may be defined by

$$e_i = \tilde{L}_{ik} \frac{dj_k}{dt}, \quad (11)$$

where j represents the current density. The following simulation results are obtained for the case of $\beta = 0$ (i.e., the adiabatic limit).

Figure 2 summarizes the magnetic textures investigated in this study and the corresponding inductance tensors. We studied four examples of helical magnetic textures, for which the helical \mathbf{q} -vector forms approximately an angle $\theta = 0^\circ, \pm 20^\circ$, and $\pm 45^\circ$ with respect to the x -direction (Fig. 2a–e, respectively); a maze-helix texture (Fig. 2f); and an SkL (Fig. 2g). The intensity and concentration of disorder were minimized as much as possible while confirming the linear response of the pinned dynamics. As a result, more disorders had to be included when examining the maze-helix and SkL, as summarized in Table 1: selecting a much lower current density while keeping the disorder density as low as 0.3% was not appropriate in terms of the required numerical accuracy. As shown in Fig. 2, we find that $\tilde{L}_{xy} = \tilde{L}_{yx}$ invariably holds within the numerical error, consistent with the conclusion derived from the circuit equations.

The diagonal components of the inductance tensor are invariably positive, whereas the off-diagonal components can be either positive or negative. Nevertheless, we emphasize that the inductance tensor retains energetic interpretations; that is, the energy increase in the magnetic system, $\Delta E(I_x, I_y)$, caused by the application of an electric current agrees with $\frac{1}{2} L_{xx} I_x^2 + \frac{1}{2} L_{yy} I_y^2 + L_{tr} I_x I_y$. As an example, we discuss the results for the helical texture with $\theta = -20^\circ$, in which the off-diagonal

components of \tilde{L}_{ij} are negative. The $\Delta E(I_x, I_y)$ is calculated for the following three cases independently: (i) ($I_x \neq 0, I_y = 0$), (ii) ($I_x = 0, I_y \neq 0$), and (iii) ($I_x \neq 0, I_y \neq 0$). Then, by solving the three simultaneous equations regarding $\Delta E(I_x, I_y) = \frac{1}{2} L_{xx} I_x^2 + \frac{1}{2} L_{yy} I_y^2 + L_{tr} I_x I_y$, we can obtain: $(\tilde{L}_{xx}, \tilde{L}_{yy}, \tilde{L}_{tr}) = (2.67, 0.63, -1.00) \times 10^{-21}$ H m. These values are in quantitative agreement with \tilde{L}_{ij} calculated from the EEF (Fig. 2c), indicating that the emergent inductivity is well defined by Eq. (11). We also confirmed $\tilde{L}_{xy}(\mathbf{B}, \mathbf{m}(\mathbf{r}_k)) = \tilde{L}_{xy}(-\mathbf{B}, -\mathbf{m}(\mathbf{r}_k))$ numerically (Fig. 3), in which the disorder density and strength K_{imp} (see “Methods”) are fixed to 3% and 1.0×10^7 J m⁻³, respectively, and the single- \mathbf{q} -helix with $\theta = 45^\circ$ was considered. Thus, our numerical study confirms that \tilde{L}_{ij} for an emergent inductor is a polar symmetric tensor.

When comparing the three helical textures quantitatively, one can find that as the θ increases from 0° to 45° , \tilde{L}_{xx} decreases, whereas \tilde{L}_{xy} increases. We also note that in the maze-helix and SkL textures, the transverse component, \tilde{L}_{xy} , is more than one order of magnitude smaller than the longitudinal components, \tilde{L}_{xx} and \tilde{L}_{yy} . As discussed below, these observations can be explained by considering an orthogonal transformation of \tilde{L}_{ij} and the rotational symmetry that each magnetic texture has.

DISCUSSION

In the following, we aim to categorize inductance tensors of a magnetic-texture origin and consider how our numerical results obtained in the adiabatic limit can be explained in terms of the symmetry operations that each magnetic system has. Note that because an inductance tensor is real and symmetric, it can be diagonalized by performing an appropriate orthogonal transformation, R , or equivalently by choosing appropriate Cartesian coordinates:

$$\begin{pmatrix} \tilde{L}_{xx} & \tilde{L}_{tr} \\ \tilde{L}_{tr} & \tilde{L}_{yy} \end{pmatrix} \xrightarrow{R} \begin{pmatrix} \lambda_1 & 0 \\ 0 & \lambda_2 \end{pmatrix}, \quad (12)$$

where λ_1 and λ_2 ($\lambda_1, \lambda_2 \geq 0$) represent the eigenvalues of the inductance tensor. Hence, to classify an emergent inductance tensor, it is sufficient to consider the diagonalized form. This approach does not lose generality because a representation in different Cartesian coordinates can be immediately obtained by performing the corresponding orthogonal transformation. Following the group theory arguments for a polar symmetric tensor, one can conclude that: (i) when the system has three-fold or higher rotational symmetry with respect to the z -axis (i.e., C_{3z}, C_{4z}, C_{6z} or $C_{\infty z}$), λ_1 and λ_2 should be equal, whereas (ii) when the system has only two-fold with respect to the z -axis (C_{2z}) or no rotational symmetry, λ_1 and λ_2 should be inequivalent: For the details of the derivation, see Supplementary Note 3. Thus, the diagonalized two-by-two tensor can be classified as one of the two categories, which are characterized by $\lambda_1 = \lambda_2$ and $\lambda_1 \neq \lambda_2$, respectively.

The first category, $\lambda_1 = \lambda_2$, is represented by an isotropic tensor $\begin{pmatrix} 1 & 0 \\ 0 & 1 \end{pmatrix}$, and thus, the off-diagonal components are always zero for arbitrarily chosen Cartesian coordinates; that is, the transverse inductance response does not appear. From group theory, a magnetic texture that has C_{3z}, C_{4z}, C_{6z} , or $C_{\infty z}$ symmetry should belong to this category. Note that our numerical calculations deal with finite-size systems including randomly distributed disorder, and therefore, the simulated magnetic textures do not have any rotational symmetry in a strict sense. Nevertheless, we numerically find that the inductance tensors of the maze-helix and SkL textures satisfy $\tilde{L}_{xx} \approx \tilde{L}_{yy}$ and $\tilde{L}_{xy}, \tilde{L}_{yx} \ll \tilde{L}_{xx}, \tilde{L}_{yy}$ (Fig. 2f, g, respectively), indicating that the obtained tensors are close to isotropic. These results appear reasonable,

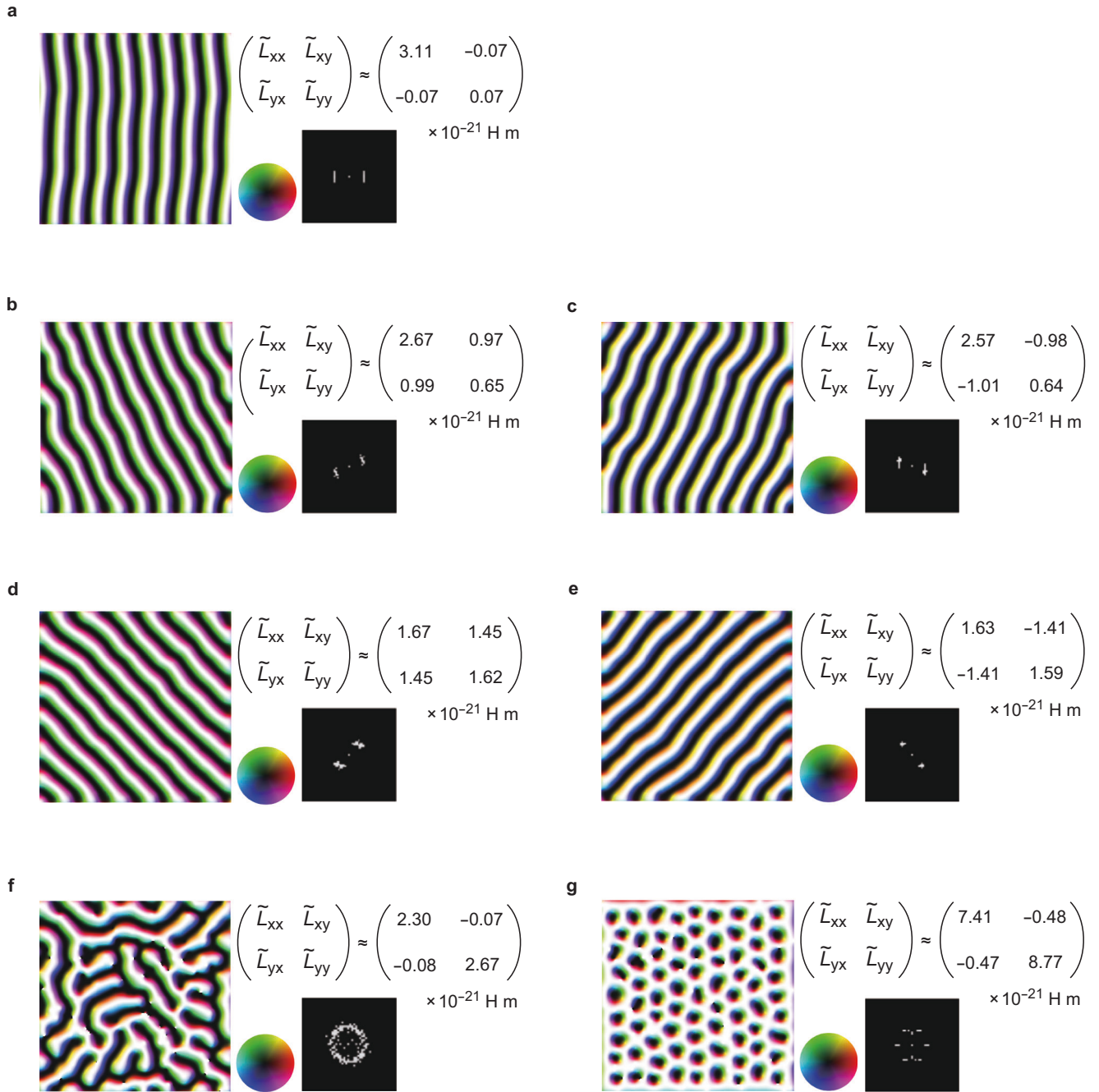


Fig. 2 Various metastable magnetic textures and corresponding inductance tensors. **a–e** Helical magnetic textures with the helical \mathbf{q} -vector that forms approximately an angle $\theta = 0^\circ$ (**a**), 20° (**b**) -20° (**c**), 45° (**d**), and -45° (**e**) with respect to the x -direction. **f** Maze-helix. **g** Skyrmion lattice. The corresponding fast-Fourier-transform (FFT) images are also shown in each panel. Color wheels specify the x - y plane magnetization direction. The brightness of the color represents the z component of the magnetization, and white represents the local magnetizations pointing toward the z -direction. The current-induced magnetic-texture dynamics are calculated under the application of a weak AC current. The parameters used for the simulation are tabulated in Table 1; they are chosen so that the resulting emergent voltage is in the linear response and low-frequency regimes (see the “Methods” section). The simulations were done for $\beta = 0$.

considering that in a macroscopic system, the maze-helix and SkL textures have global approximate $C_{\infty z}$ and C_{6z} symmetries, respectively. The symmetry of the macroscopic systems can be imagined by looking at the corresponding fast-Fourier-transform (FFT) images. To be precise, the rotation symmetry of the SkL confined in the finite-size system is C_{2z} , rather than C_{6z} , as indicated by the FFT image (Fig. 2g): This perturbative symmetry lowering from C_{6z} to C_{2z} explains the small but finite symmetric off-diagonal component, which is originally prohibited under C_{6z}

symmetry. When nonadiabaticity is not negligible, the effective inductivity tensor defined by $\tilde{L}_{ij}^{\text{eff}} = \text{Im}[\rho_{ij}(\omega) - \rho_{ij}(0)]/\omega$ is discussed, but it should be noted that $\tilde{L}_{ij}^{\text{eff}}$ is a different quantity from the inductivity tensor in Eq. (11). For instance, the $\tilde{L}_{ij}^{\text{eff}}$ of the SkL has antisymmetric off-diagonal components when $\beta \neq 0$, although the antisymmetric component in \tilde{L}_{ij} is energetically prohibited; for more details, see Supplementary Notes 1 and 3.

Table 1. Parameters used for the micromagnetic simulations displayed in Fig. 2.

Magnetic texture	Magnetic field (T)	K_{imp} ($\times 10^7 \text{ J m}^{-3}$)	Disorder density (%)	Current density ($\times 10^{10} \text{ A m}^{-2}$)	Frequency (MHz)
Helix ($\theta = 0, \pm 20^\circ, \pm 45^\circ$)	0	0.1	0.3	5.0	50
Maze-helix	0	2.0	3	2.0	50
SkL	0.3	1.0	3	1.0	10

The disorder density was chosen as low as possible while confirming the linear response of the pinned magnetic textures under a given current density.

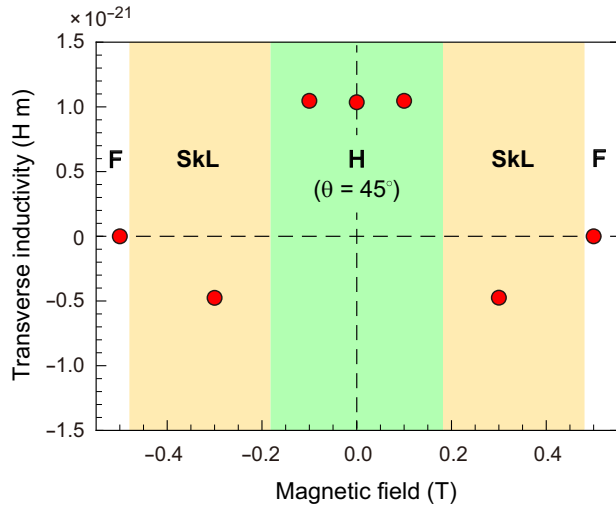


Fig. 3 Magnetic-field dependence of the transverse inductivity. H, SkL, and F denote the single- \mathbf{q} -helix with $\theta = 45^\circ$, skyrmion lattice, and ferromagnetic state, respectively. The disorder density and strength K_{imp} (see “Methods”) is fixed to 3% and $1.0 \times 10^7 \text{ J m}^{-3}$, respectively. The simulations were done for $\beta = 0$. When β is non-zero, the effective inductivity tensor $\tilde{L}_{ij}^{\text{eff}}$ should be discussed ($\tilde{L}_{ij}^{\text{eff}} = \text{Im} [\rho_{ij}(\omega) - \rho_{ij}(0)]/\omega$): The magnetic-field dependence of the transverse components of $\tilde{L}_{ij}^{\text{eff}}$ at finite β is shown in Fig. S1 and discussed in Supplementary Note 2. Note that $\tilde{L}_{ij}^{\text{eff}}$ is a different quantity from the inductivity tensor defined by Eq. (11).

The second category consists of tensors that have two inequivalent components, $\begin{pmatrix} \lambda_1 & 0 \\ 0 & \lambda_2 \end{pmatrix}$, and thus, off-diagonal components can appear if arbitrary Cartesian coordinates are chosen. For instance, the matrix $R(\theta)$ that rotates Cartesian coordinates clockwise by θ transforms the diagonalized tensor into a nondiagonal form:

$$\begin{pmatrix} \lambda_1 & 0 \\ 0 & \lambda_2 \end{pmatrix} \xrightarrow{R(\theta)} \begin{pmatrix} \lambda_1 \cos^2 \theta + \lambda_2 \sin^2 \theta & (\lambda_1 - \lambda_2) \sin \theta \cos \theta \\ (\lambda_1 - \lambda_2) \sin \theta \cos \theta & \lambda_1 \sin^2 \theta + \lambda_2 \cos^2 \theta \end{pmatrix}. \quad (13)$$

Thus, $\tilde{L}_{xy} = \tilde{L}_{yx}$ can be either positive or negative depending on the selection of Cartesian coordinates. An example of this category is a single- \mathbf{q} -helix, in which the inductance tensor is diagonalized, for instance, when the x -axis is chosen parallel to the helical \mathbf{q} -vector. An important feature of an ideal single- \mathbf{q} -helix is that the local magnetic moments show no modulation along the direction perpendicular to \mathbf{q} . Hence, no STT effect is expected for the current along the y -axis, resulting in $\lambda_2 = 0$. Thus, for the case of an ideal single- \mathbf{q} -helix, the diagonalized form and its orthogonal

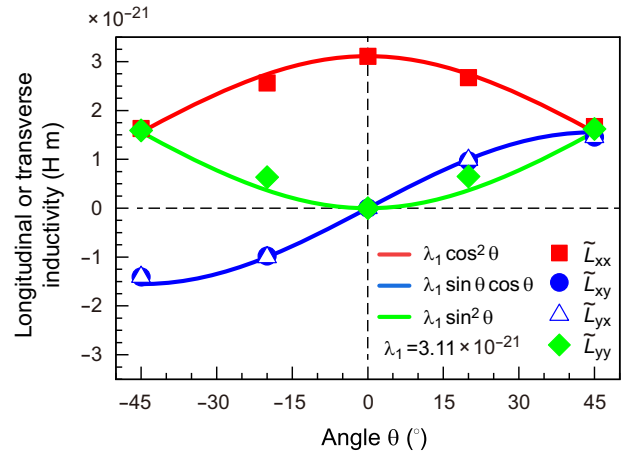


Fig. 4 Numerically obtained inductivity tensors of helical magnetic textures for various \mathbf{q} -directions. The $\theta = 0$ represents the \mathbf{q} -direction parallel to the x -axis. The solid symbols are the data obtained by the micromagnetic simulations, and the solid curves represent the corresponding trigonometric functions multiplied by $\lambda_1 = 3.11 \times 10^{-21} \text{ H m}$. The simulations were done for $\beta = 0$.

transformation are given as:

$$\begin{pmatrix} 1 & 0 \\ 0 & 0 \end{pmatrix} \xrightarrow{R(\theta)} \begin{pmatrix} \cos^2 \theta & \sin \theta \cos \theta \\ \sin \theta \cos \theta & \sin^2 \theta \end{pmatrix}. \quad (14)$$

Figure 4 displays the comparison between the numerically obtained inductivity tensors of various \mathbf{q} -direction helices and the orthogonal transformation of $\lambda_1 = 3.11 \times 10^{-21} \text{ H m}$ and $\lambda_2 = 0$, which is an approximate inductivity tensor of the single- \mathbf{q} -helix with $\theta = 0^\circ$ (Fig. 2a). Although the simulated single- \mathbf{q} -helices are more or less affected by random disorder and the open boundaries of the system, the overall tendency is well reproduced by orthogonal transformation. This observation demonstrates that the above arguments based on the orthogonal transformation of the symmetric inductivity tensor are helpful when considering a single- \mathbf{q} -helix with arbitrary \mathbf{q} -direction.

For a more complicated magnetic texture, positive λ_1 and λ_2 with $\lambda_1 \neq \lambda_2$ may be expected. For instance, a multidomain of single- \mathbf{q} -helices obviously belongs to this category. In contrast, a long-range ordered state belonging to this category may not be so clear. A candidate of this category is likely a magnetic texture that has multiple \mathbf{q} vectors with different wavenumbers, such as those observed in EuAg_4As_2 ³⁴ and EuAl_4 ³⁵; however, such an anisotropic magnetic texture is beyond the scope of our model Hamiltonian based on the continuum approximation [see Eq. (15) in the “Methods” section].

To conclude, we have revealed analytically and numerically the symmetry of the emergent inductance tensor exhibited by pinned magnetic textures. We focused on the adiabatic limit, where the

inductance tensor is well defined by $e_i = \tilde{L}_{ik} \frac{dj_k}{dt}$. We thus found that the inductance tensor is a real symmetric tensor, and hence, the presence and magnitude of the transverse component are determined by the degree to which the measurement axis is tilted from the principal axis that generates the diagonalized tensor. As a natural consequence of the real symmetric tensor, the transverse component does not change sign with respect to the magnetic-field reversal. These fundamental aspects of the emergent inductance tensor will be useful when exploring the transverse inductive response in a magnetic texture. However, it must also be noted that when nonadiabaticity is not negligible, the electric response produced by magnetic textures may not be described by an inductance tensor in the strict sense defined by Eq. (4).

METHODS

Numerical model

In this study, we consider long-period helical magnetic textures that are stabilized by the Dzyaloshinskii–Moriya (DM) interaction^{36,37}. We consider dirty systems including randomly distributed disorder. Our model Hamiltonian is:

$$\mathcal{H} = \int \frac{d^3r}{a^3} \left[\frac{J}{2} (\nabla \mathbf{m})^2 + D \mathbf{m} \cdot (\nabla \times \mathbf{m}) \right] - \sum_{k \in \Lambda} \int_{V_k} d^3r K_{\text{imp}} (\mathbf{m}_k \cdot \mathbf{n}_{\text{imp},k})^2 \quad (15)$$

where J is the Heisenberg exchange energy, D is the DM interaction and a is the lattice constant. The extrinsic pinning effect is controlled by the last term of Eq. (15), which is introduced to randomly selected cells to break the translational symmetry: $K_{\text{imp}} (> 0)$ represents the magnetic-easy-axis anisotropy along a randomly chosen direction, $\mathbf{n}_{\text{imp},k}$, at the k -th cell (the cell volume V_k is 3^3 nm^3), and Λ is a set of random numbers. The disorder density displayed in Table 1 represents the ratio of the number of cells with finite K_{imp} to the total number of cells (243×243).

When simulating the current-induced dynamics of a given helical magnetic structure, we insert the spin Hamiltonian into the following Landau–Lifshitz–Gilbert (LLG) equation³³:

$$\frac{d\mathbf{m}_r(t)}{dt} = -\frac{|\gamma|}{1+a^2} \frac{d\mathcal{H}}{d\mathbf{m}_r} \times \mathbf{m}_r - \frac{a|\gamma|}{1+a^2} \left[\mathbf{m}_r \times \left(\frac{d\mathcal{H}}{d\mathbf{m}_r} \times \mathbf{m}_r \right) \right] + \frac{1}{1+a^2} \{ (1+\beta a) \mathbf{m}_r \times [\mathbf{m}_r \times (\mathbf{u} \cdot \nabla) \mathbf{m}_r] + (\beta - a) [\mathbf{m}_r \times (\mathbf{u} \cdot \nabla) \mathbf{m}_r] \}, \quad (16)$$

where \mathbf{u} represents the spin drift velocity, a is the Gilbert damping constant, β is a dimensionless constant that characterizes the nonadiabatic electron spin dynamics, and $\gamma (> 0)$ is the gyromagnetic ratio; \mathbf{u} is related to the electric current density \mathbf{j} by $\mathbf{u} = \frac{P\mu_B}{2|e|M_s(1+\beta^2)} \mathbf{j}$, where μ_B is the Bohr magneton and M_s is the saturation magnetization. When implementing the micromagnetic simulation, we use the open software MuMax3 (<https://mumax.github.io/download.html>)³⁸. We choose the following parameter set: $J/(2a^3) = 1.8 \times 10^{-11} \text{ J m}^{-1}$, $D/a^3 = 2.8 \times 10^{-3} \text{ J m}^{-2}$, $M_s = 2.45 \times 10^5 \text{ A m}^{-1}$, $P = 1$, and $a = 0.04$.

In the simulation, we apply a current density of a sufficiently small magnitude so that the magnetic system is certainly in the linear-response regime; that is, with respect to the input alternating electric current along the x - or y -direction, $j_i(t) = j_{0,i} \sin \omega t$ ($i = x, y$), the magnetic system is in the pinned regime, and the output AC emergent voltage, $V_{e,i}(t)$, is $\propto j_{0,k} \omega \cos \omega t$ ($i, k = x, y$). Based on these observations, L_{ij} is derived from the following equations:

$$V_{e,i}(t) = \langle e_i(t) \rangle \ell = L_{ij} \frac{d(j_j(t))}{dt}, \quad (17)$$

where $\langle \dots \rangle$ denotes a spatially averaged value, the system length ℓ is $243 \times 3 \text{ nm}$, and $l = jS$ with the cross-section area $S = 243 \times 1 \times 3^2 \text{ nm}^2$. In the present frequency range ($\leq 100 \text{ MHz}$), it is confirmed that the inductivity is independent of ω (i.e., $\langle e_i \rangle \propto \omega$) (Fig. S2) and the a dependence of the numerical results is negligibly small (Fig. S3) (see also Supplementary Note 4). The numerical accuracy of MuMax3 is $\Delta \mathbf{m}/|\mathbf{m}| \sim 10^{-7}$, and the typical increment of $\Delta \mathbf{m}/|\mathbf{m}|$ in one time step (4 ps) is $\sim 10^{-5}$ under the current application of $\sim 10^{10} \text{ A m}^{-2}$. This finite accuracy eventually gives rise to an uncertainty of $\sim 10^{-23} \text{ H m}$ in the calculated inductivity.

In the numerical simulation, a uniform current density is considered to understand fundamental aspects of the inductivity tensor. On the other hand, the local ρ_{xx} and ρ_{yx} may be non-uniform in real material, reflecting spatial variations in magnetic textures. Nevertheless, the uniform current is a good approximation as long as $\langle \rho_{xx} \rangle \gg \delta \rho_{xx}, \delta \rho_{yx}$, where $\delta \rho_{xx}$ and $\delta \rho_{yx}$ represent the magnitude of the spatial variations. For instance, in the chiral magnet MnSi at 10 K, the presence or absence of the metastable skyrmion lattice changes ρ_{xx} and ρ_{yx} by $\approx 50 \text{ n}\Omega \text{ cm}$ and $\approx 30 \text{ n}\Omega \text{ cm}$, respectively, whereas $\rho_{xx} \approx 5 \mu\Omega \text{ cm}$ ³⁹. Such magnetic-texture-dependent ρ_{xx} and ρ_{yx} imply that $\langle \rho_{xx} \rangle \gg \delta \rho_{xx}, \delta \rho_{yx}$ holds, although the precise estimation of the spatial variations is experimentally difficult; thus, the current uniformity is well expected. If $\delta \rho_{xx}$ and $\delta \rho_{yx}$ are significant, the current distribution should be determined self-consistently; for instance, see ref. 40.

Initial-state preparation

To obtain various metastable magnetic textures, a pristine helical texture with a different oblique angle of the helical \mathbf{q} -vector, a random spin configuration, or a SkL is prepared as an initial state and then relaxed under zero current. Note that imposing the open-boundary condition and introducing disorder are key in obtaining the intended magnetic textures.

DATA AVAILABILITY

The data used in this work are available from the corresponding author upon reasonable request.

Received: 3 August 2023; Accepted: 11 October 2023;

Published online: 22 November 2023

REFERENCES

- Jackson, J. D. *Classical Electrodynamics*. 3rd edn. (Wiley, 1998).
- Kang, J. et al. On-chip intercalated-graphene inductors for next-generation radio frequency electronics. *Nat. Elec.* **1**, 46–51 (2018).
- Nagaosa, N. Emergent inductor by spiral magnets. *Jpn. J. Appl. Phys.* **58**, 120909 (2019).
- Yokouchi, T. et al. Emergent electromagnetic induction in a helical-spin magnet. *Nature* **586**, 232 (2020).
- Kitaori, A. et al. Emergent electromagnetic induction beyond room temperature. *Proc. Natl. Acad. Sci. USA* **118**, e2105422118 (2021).
- Kitaori, A. et al. Doping control of magnetism and emergent electromagnetic induction in high-temperature helimagnets. *Phys. Rev. B* **107**, 024406 (2023).
- Slonczewski, J. C. Current-driven excitation of magnetic multilayer. *J. Magn. Mater.* **159**, L1–L7 (1996).
- Berger, L. Emission of spin waves by a magnetic multilayer traversed by a current. *Phys. Rev. B* **54**, 9353–9358 (1996).
- Yamanouchi, M., Chiba, D., Matsukura, F. & Ohno, H. Current-induced domain-wall switching in a ferromagnetic semiconductor structure. *Nature* **428**, 539–542 (2004).
- Yamaguchi, A. et al. Real-space observation of current-driven domain wall motion in submicron magnetic wires. *Phys. Rev. Lett.* **92**, 077205 (2004).
- Volovik, G. E. Linear momentum in ferromagnets. *J. Phys. C* **20**, L83–L87 (1987).
- Barnes, S. E. & Maekawa, S. Generalization of Faraday's law to include non-conservative spin forces. *Phys. Rev. Lett.* **98**, 246601 (2007).

13. Yang, S. A. et al. Universal electromotive force induced by domain wall motion. *Phys. Rev. Lett.* **102**, 067201 (2009).
14. Zang, J., Mostovoy, M., Han, J. H. & Nagaosa, N. Dynamics of skyrmion crystals in metallic thin films. *Phys. Rev. Lett.* **107**, 136804 (2011).
15. Schulz, T. et al. Emergent electrodynamics of skyrmions in a chiral magnet. *Nat. Phys.* **8**, 301–304 (2012).
16. Furuta, S., Moody, S. H., Kado, K., Koshibae, W. & Kagawa, F. Energetic perspective on emergent inductance exhibited by magnetic textures in the pinned regime. *npj Spintronics* <https://doi.org/10.1038/s44306-023-00004> (2023).
17. Feynman, R. P., Leighton, R. B. & Sands, M. L. *The Feynman Lectures on Physics, Vol. II* (Basic Books, 2011).
18. Kubo, R. Statistical-mechanical theory of irreversible processes. I. *J. Phys. Soc. Jpn.* **12**, 570–586 (1957).
19. Nattermann, T., Shapir, Y. & Vilfan, I. Interface pinning and dynamics in random systems. *Phys. Rev. B* **42**, 8577–8586 (1990).
20. Chauve, P., Giamarchi, T. & Doussal, P. L. Creep and depinning in disordered media. *Phys. Rev. B* **62**, 6241–6267 (2000).
21. Kleemann, W. Universal domain wall dynamics in disordered ferroic materials. *Annu. Rev. Mater. Res.* **37**, 415–448 (2007).
22. Tataru, G. & Kohno, H. Theory of current-driven domain wall motion: spin transfer versus momentum transfer. *Phys. Rev. Lett.* **92**, 086601 (2004).
23. Thiaville, A., Nakatani, Y., Miltat, J. & Suzuki, Y. Micromagnetic understanding of current-driven domain wall motion in patterned nanowires. *Europhys. Lett.* **69**, 990–996 (2005).
24. Tataru, G. et al. Threshold current of domain wall motion under extrinsic pinning, β -term and non-adiabaticity. *J. Phys. Soc. Jpn.* **75**, 064708 (2006).
25. Koyama, T. et al. Observation of the intrinsic pinning of a magnetic domain wall in a ferromagnetic nanowire. *Nat. Mat.* **10**, 194–197 (2011).
26. Tataru, G., Kohno, H. & Shibata, J. Microscopic approach to current-driven domain wall dynamics. *Phys. Rep.* **468**, 213–301 (2008).
27. Burrowes, C. et al. Non-adiabatic spin-torques in narrow magnetic domain walls. *Nat. Phys.* **6**, 17–21 (2010).
28. Iwasaki, J., Mochizuki, M. & Nagaosa, N. Universal current-velocity relation of skyrmion motion in chiral magnets. *Nat. Commun.* **4**, 1463 (2013).
29. Bogdanov, A. & Yablonskii, D. A. Thermodynamically stable “vortices” in magnetically ordered crystals. The mixed state of magnets. *Sov. Phys. JETP* **68**, 101–103 (1989).
30. Bogdanov, A. & Hubert, A. Thermodynamically stable magnetic vortex states in magnetic crystals. *J. Magn. Magn. Mater.* **138**, 255–269 (1994).
31. Mühlbauer, S. et al. Skyrmion lattice in a chiral magnet. *Science* **323**, 915–919 (2009).
32. Yu, X. Z. et al. Real-space observation of a two-dimensional skyrmion crystal. *Nature* **465**, 901–904 (2010).
33. Zhang, S. & Li, Z. Roles of nonequilibrium conduction electrons on the magnetization dynamics of ferromagnets. *Phys. Rev. Lett.* **93**, 127204 (2004).
34. Shen, B. et al. Structural distortion and incommensurate noncollinear magnetism in EuAg_4As_2 . *Phys. Rev. Mater.* **4**, 064419 (2020).
35. Takagi, R. et al. Square and rhombic lattices of magnetic skyrmions in a centrosymmetric binary compound. *Nat. Commun.* **13**, 1472 (2022).
36. Dzyaloshinskii, I. A thermodynamic theory of “weak” ferromagnetism of antiferromagnetics. *J. Phys. Chem. Solids* **4**, 241–255 (1958).
37. Moriya, T. Anisotropic superexchange interaction and weak ferromagnetism. *Phys. Rev.* **120**, 91–98 (1960).
38. Vansteenkiste, A. et al. The design and verification of MuMax3. *AIP Adv.* **4**, 107133 (2014).
39. Oike, H. et al. Topological Nernst effect emerging from real-space gauge field and thermal fluctuations in a magnetic skyrmion lattice. *Phys. Rev. B* **106**, 214425 (2022).
40. Bourianoff, G., Pinna, D., Sitte, M. & Everschor-Sitte, K. Potential implementation of reservoir computing models based on magnetic skyrmions. *AIP Adv.* **8**, 055602 (2018).

ACKNOWLEDGEMENTS

The authors thank N. Nagaosa and Y. Fujishiro for their valuable discussions. This work was partially supported by JSPS KAKENHI (Grants No. 20K03810, No. 18H05225, No. 23K03291, and No. 21H04442), JST CREST (Grants No. JPMJCR1874 and No. JPMJCR20T1).

AUTHOR CONTRIBUTIONS

S.F. conducted the calculations and analyzed the data. F.K. conceived the project and wrote the draft with S.F. and W.K. All the authors discussed the results and commented on the manuscript.

COMPETING INTERESTS

The authors declare no competing interests.

ADDITIONAL INFORMATION

Supplementary information The online version contains supplementary material available at <https://doi.org/10.1038/s44306-023-00001-4>.

Correspondence and requests for materials should be addressed to Fumitaka Kagawa.

Reprints and permission information is available at <http://www.nature.com/reprints>

Publisher's note Springer Nature remains neutral with regard to jurisdictional claims in published maps and institutional affiliations.



Open Access This article is licensed under a Creative Commons Attribution 4.0 International License, which permits use, sharing, adaptation, distribution and reproduction in any medium or format, as long as you give appropriate credit to the original author(s) and the source, provide a link to the Creative Commons license, and indicate if changes were made. The images or other third party material in this article are included in the article's Creative Commons license, unless indicated otherwise in a credit line to the material. If material is not included in the article's Creative Commons license and your intended use is not permitted by statutory regulation or exceeds the permitted use, you will need to obtain permission directly from the copyright holder. To view a copy of this license, visit <http://creativecommons.org/licenses/by/4.0/>.

© The Author(s) 2023